Journal of Biomedical Optics

SPIEDigitalLibrary.org/jbo

Spatially resolved optical and ultrastructural properties of colorectal and pancreatic field carcinogenesis observed by inverse spectroscopic optical coherence tomography

Ji Yi
Andrew J. Radosevich
Yolanda Stypula-Cyrus
Nikhil N. Mutyal
Samira Michelle Azarin
Elizabeth Horcher
Michael J. Goldberg
Laura K. Bianchi
Shailesh Bajaj
Hemant K. Roy
Vadim Backman

SPIE

Spatially resolved optical and ultrastructural properties of colorectal and pancreatic field carcinogenesis observed by inverse spectroscopic optical coherence tomography

Ji Yi,[a] Andrew J. Radosevich,[a] Yolanda Stypula-Cyrus,[a] Nikhil N. Mutyal,[a] Samira Michelle Azarin,[a] Elizabeth Horcher,[a] Michael J. Goldberg,[c] Laura K. Bianchi,[c] Shailesh Bajaj,[c] Hemant K. Roy,[b] and Vadim Backman[a,*]

[a]Northwestern University, Department of Biomedical Engineering, 2145 Sheridan Road, Evanston, Illinois 60208
[b]Boston Medical Center, Department of Medicine, Boston, Massachusetts 02118
[c]NorthShore University Health Systems, Department of Internal Medicine, Evanston, Illinois 60201

Abstract. Field carcinogenesis is the initial stage of cancer progression. Understanding field carcinogenesis is valuable for both cancer biology and clinical medicine. Here, we used inverse spectroscopic optical coherence tomography to study colorectal cancer (CRC) and pancreatic cancer (PC) field carcinogenesis. Depth-resolved optical and ultrastructural properties of the mucosa were quantified from histologically normal rectal biopsies from patients with and without colon adenomas ($n = 85$) as well as from histologically normal peri-ampullary duodenal biopsies from patients with and without PC ($n = 22$). Changes in the epithelium and stroma in CRC field carcinogenesis were separately quantified. In both compartments, optical and ultra-structural alterations were consistent. Optical alterations included lower backscattering (μ_b) and reduced scattering (μ_s') coefficients and higher anisotropy factor g. Ultrastructurally pronounced alterations were observed at length scales up to ~450 nm, with the shape of the mass density correlation function having a higher shape factor D, thus implying a shift to larger length scales. Similar alterations were found in the PC field carcinogenesis despite the difference in genetic pathways and etiologies. We further verified that the chromatin clumping in epithelial cells and collagen cross-linking caused D to increase *in vitro* and could be among the mechanisms responsible for the observed changes in epithelium and stroma, respectively. [DOI: 10.1117/1.JBO.19.3.036013]

Keywords: colorectal; pancreatic; field carcinogenesis; ultrastructural; optical properties.

Paper 130508RRRR received Jul. 18, 2013; revised manuscript received Feb. 13, 2014; accepted for publication Feb. 17, 2014; published online Mar. 18, 2014.

1 Introduction

Cancer progression is a multistep process that develops through a number of stages, including dysplasia, tumorigenesis, and metastases. One of the earliest stages is field carcinogenesis (also referred to as field cancerization, field effect, field of injury, field defect, etc.), the concept that a diffuse injury from genetic/environmental stimuli provides a fertile mutational field with focal tumorigenesis occurring via stochastic events such as inactivation of tumor suppressor genes.[1,2] The concept of field carcinogenesis is well established in cancer biology and clinical medicine and has been observed in essentially all solid cancers (lung,[3] colon and rectum,[4,5] prostate,[6,7] esophageal,[8] pancreatic,[9] ovarian, head and neck,[10] stomach,[11] and breast[12]). It provides the biological underpinning of the occurrence of both synchronous (multiple tumors in the organ) and metachronous (recurrent neoplasia elsewhere in the organ) lesions. Because field carcinogenesis provides the key to tumor initiation, it has relevance not only for clinical medicine, but also for fundamental cancer biology.

During field carcinogenesis, an affected organ typically appears to be grossly and histologically normal under a conventional microscope with no visible macro- or microscopic structural changes. Undetectable by histopathology, however, the initial molecular and ultrastructural alterations have already occurred. (The term "ultrastructure" refers to tissue morphology that is below the resolution of microscopic histopathology and encompasses the suborganelles and macromolecular length scales—typically on the order of several hundreds of nanometers and below and down to a few tens of nanometers.) Because these length scales are unresolvable by a conventional microscope, there is a need to develop other methods to detect such early alterations.

A number of optical techniques have been previously reported for studying field carcinogenesis in various cancers. Raman scattering has been developed in combination with classification methods to detect the risk of cervical and skin cancers.[13,14] Karyometric analysis was used to assess nuclear chromatin patterns in colorectal cancer (CRC) field carcinogenesis.[15] Fourier-domain low-coherence interferometry (fLCI) has been used to investigate the cell nuclear size changes in colon mucosa on a CRC animal model.[16] Elastic scattering spectroscopy (ESS) of uninvolved mucosa has been reported to detect the CRC cancer risk.[17] Low coherence-enhanced backscattering (LEBS) spectroscopy has also been applied to demonstrate the field carcinogenesis in CRC, pancreatic cancer (PC), and lung cancer *ex vivo* and *in vivo*.[18–21] Enhanced backscattering (EBS)

*Address all correspondence to: Vadim Backman, E-mail: v-backman@northwestern.edu

spectroscopy has been used to study ultrastructural alterations in CRC and PC field effects *ex vivo*.[22] These earlier studies have shown the promise of an optical detection of field carcinogenesis for early cancer screening applications (e.g., LEBS) and diagnosis (e.g., fLCI and ESS). However, a comprehensive analysis of the optical and ultrastructural alterations associated with field carcinogenesis in the two major tissues comprising the mucosa, i.e., the epithelium and stroma [extracellular matrix (ECM) in particular] is still lacking.

Here, we use inverse spectroscopic optical coherence tomography (ISOCT)[23–26] to provide a quantification of the ultrastructural alterations in epithelium and stroma in field carcinogenesis. Optical coherence tomography (OCT) conventionally has been used to provide the microscopic reconstruction of tissue morphology with a spatial resolution on the order of several microns.[27,28] It has also been used to quantify optical properties of bulk tissue including scattering coefficient,[29–32] backscattering coefficient,[33,34] anisotropy factor,[29,35] and absorption coefficient.[36,37] The ISOCT models the tissue as a medium with a continuously varying refractive index (RI). By measuring its optical properties, the RI correlation function can be inversely recovered. Because of the linear relationship between RI and macromolecular mass density, ISOCT is then able to quantify the ultrastructural properties underlying the optical properties at each three-dimensional (3-D) OCT voxel of spatial resolution.[24] Moreover, because ISOCT utilizes the spectral information to measure the self-interference within a resolution-limited voxel, the length scale of sensitivity of ISOCT can be as small as ~35 nm, far beyond the resolution limit of conventional microscopy.[23,38]

In this article, we apply ISOCT to address three specific questions about field carcinogenesis: (1) In which mucosal compartment (i.e., epithelium versus ECM) do changes occur? (2) What are the associated ultrastructural alterations that occur within each of these compartments? and (3) What are some of the specific mechanisms that contribute to these ultrastructural alterations? To answer these questions, we studied the optical and ultrastructural changes in CRC field carcinogenesis and separately analyzed the epithelium and stroma compartments. Furthermore, considering that the histological alterations are a universal marker of carcinogenesis in essentially all types of cancer, we tested whether the optical and ultrastructural alterations are specific to CRC field carcinogenesis or could potentially represent a more ubiquitous event pertinent to field carcinogenesis in other organs. Therefore, we studied optical and ultrastructural alterations in PC field carcinogenesis for comparison. *Ex vivo* biopsies from the rectum and peri-ampullary duodenum (i.e., a portion of the duodenum in close proximity to the opening of the pancreatic duct) were used as the surrogate sites for CRC and PC fields carcinogenesis, respectively. Furthermore, we used *in vitro* models to investigate whether chromatin clumping and collagen cross-linking, two of the most common hallmarks of structural changes in cancer, could contribute to the ultrastructural alterations in field carcinogenesis.

The article is organized as follows: in Sec. 2, we provide an in-depth review of the biological background and significance of the study; in Sec. 3, we introduce the theory of modeling tissue as a continuously varying RI medium and the inverse model for ISOCT; in Sec. 4, the methods of the study are explained; Sec. 5 presents the results; Sec. 6 is the discussion; and Sec. 7 is the conclusion.

2 Biological Background and Significance

The terminology of the different stages of carcinogenesis has been introduced by pathologists through either a gross or microscopic (histopathologic) examination of tumors and precancerous lesions. Histopathology has been the gold standard for cancer diagnosis for the past century and will remain so for the foreseeable future, despite an ongoing revolution in our understanding of the molecular underpinnings of the disease. The reason is, to a large extent, because morphological (structural) alterations are a common denominator of essentially all molecular pathways and essentially all cancer types. While there are hundreds of genetic events and more than a dozen of distinct molecular pathways that have been implicated in carcinogenesis in a given organ site, essentially all neoplasms share the same few morphological alterations. The morphological hallmarks of neoplasia include both intracellular and ECM alterations. A key cellular marker is nuclear atypia, in particular abnormal chromatin clumping and hyperchromatism. With regard to ECM events, collagen cross-linking leading to an increase in the ECM stiffness is an ubiquitous event in the tumor microenvironment.

The sequence from field carcinogenesis to dysplasia to carcinoma to metastases is driven by the development of molecular as well as morphological alterations at progressively larger length scales. A carcinoma is frequently a macroscopically detectable lesion with morphological alterations at both macro- and microscales. At an earlier stage, dysplasia is a term used to describe a precancerous, early neoplastic process based on the microscopic appearance of cells. While some dysplastic lesions may have macroscopic manifestations (e.g., colon adenomas), the majority are defined exclusively based on their micromorphology (e.g., colon flat dysplasia and cervical dysplasia). In either case, micromorphology is the defining characteristic. At an even earlier stage, field carcinogenesis does not exhibit microscopic abnormalities and the tissue appears histologically normal. At this stage, however, the tissue does possess multiple molecular as well as submicroscopic or ultrastructural alterations.

A myriad of molecular alterations in field carcinogenesis has been reported, including biochemical (e.g., protein kinase C activity,[39] ornithine decarboxylase,[40] and mucus disaccharide content[41]), immunohistochemical (the loss of cytochrome C oxidase subunit I[42]), cellular (proliferation[43] and apoptosis[44]), genomic [tumor suppress gene p53,[3,10] cyclooxygenase 2, osteopontin,[45] the loss of imprinting of insulin growth factor (IGF)-2,[46,47] tumor growth factor(TGF)-α,[48] and IGF binding protein 3[49]], proteomic,[50] microvasculature (increased blood supply,[51–53] the expression of pro-angiogenic proteins such as COX-2, iNOS, VEGF, and osteopontin, germline vascular polymorphisms such as VEGF and Eng-1[54]), and epigenomic (abnormal methylation[55,56] and histone acetylation[57,58]) markers.

Many of these molecular events in field carcinogenesis have ultrastructural consequences. Indeed, ultrastructural, epigenetic, genetic, and other molecular events in carcinogenesis are inherently interdependent. For instance, the altered DNA methylation (an epigenetic event)[55] changes the higher-order chromatin structure (an ultrastructural event),[59] which in turn affects the gene expression (genetic alterations).[56,60]

One recent insight into the development of carcinomas is that there is both an epithelial and stromal components. In fact, cross-talk from the stroma is critical for all phases of neoplastic transformation. One essential question on the mechanisms

underlying the development of field carcinogenesis is this: In which tissue compartment do the initial molecular/ultrastructural alterations drive field carcinogenesis, epithelium or stroma, or both? One theory is that the genomic and epigenomic alterations in epithelial cells at this premalignant stage drive field carcinogenesis. However, there are emerging data suggesting that the stroma not only reciprocates the epithelial changes, but may also potentiate the epithelial changes in field carcinogenesis.[61,62] For example, transgenic mice with transforming growth factor β type II receptor knockdown restricted to the stroma still had evidence of malignant transformation of the epithelium.[63] While these earlier studies demonstrate the importance of epithelium-stroma cross-talk in cancer, the exact contribution from the two compartments in human field carcinogenesis remains unknown. Given the biological context of field carcinogenesis, the study presented here addresses the ultrastructural changes in the epithelium and stroma separately.

3 Theory

3.1 *Continuously Varying RI Model for Tissue and Corresponding Optical Properties*

Optical scattering originates from spatial heterogeneity in the RI of biological tissue. To model this heterogeneity, a number of approaches have been proposed. In one popular representation, tissue is treated as a collection of homogeneous spheres (or spheroids) of various sizes (discrete particle model).[64,65] The total scattering is then an incoherent summation of the scattered intensity from all spheres. Those models provide reasonably accurate representations for cellular components such as the cell nucleus, mitochondria, and ribosomes, which arguably resemble discrete spheres/spheroids. The shortcomings of the discrete particle model are that the complex inner structure of organelles is neglected, as well as the interaction between scatterers, and the model is not able to accurately represent ECM network structures. In fact, most tissue components are interconnected instead of being isolated and discrete; and within organelles, the inner structures are spatially heterogeneous rather than being homogeneous.

An alternative approach is to model tissue as a continuously varying RI medium.[66–70] A comprehensive way to quantify such a medium is by using the RI autocorrelation function to calculate the correlation of RI between any two points in 3-D space with a spatial separation r_d. Since the exact RI correlation function of tissue has not yet been accurately measured and may vary significantly among different tissue types, we instead used the versatile three-parameter Whittle–Matèrn (W–M) family of correlation functions to model the spatial distribution of RI in tissue[66,70]

$$B_n(r_d) = A_n \left(\frac{r_d}{L_n}\right)^{(D-3)/2} K_{(D-3)/2}\left(\frac{r_d}{L_n}\right), \tag{1}$$

where $K_{\{\cdot\}}$ is the modified Bessel function of the second type; A_n is the amplitude of the RI fluctuation; D is the functional "shape factor" determining the type of the function; and L_n is the length scale of the correlation function whose exact meaning depends on D. Table 1 lists the functional type for different D values. When $0 < D < 3$, the correlation function is a power law and the tissue is organized as a mass fractal. D is then the mass fractal dimension D_f. For $D < 3$, L_n defines the upper length scale of the mass fractal range. For $D = 4$, $B_n(r_d)$ is an exponential function and L_n is its correlation length, where $B_n(L_n) = B_n(0)\, e^{-1}$. The physical meaning of A_n also depends on D. A definition of an RI correlation function requires a normalization such that at the origin ($r_d = 0$), the function is equal to the variance of the RI fluctuation σ_n^2. For $D \le 3$, the W–M correlation function approaches infinity at the origin. One way to keep the functional form bounded is to introduce another lower limit of length scale $r_{\min}$ below which the function levels to the origin, as in Eq. (2). The value of $r_{\min}$ could be chosen to be the lower limit of the length scale of sensitivity, since it is no longer sensitive to any structural perturbations smaller than $r_{\min}$. For $D > 3$, the W–M correlation functions are naturally bounded at the origin, and thus A_n can be analytically associated with σ_n^2.

Table 1 *D* dependent functional type.

D	Functional shape
0 to 3	Power law
3 to 4	Stretched exponential
4	Exponential
∞ (Inf)	Gaussian

$$\sigma_n^2 = \begin{cases} A_n \times 2^{(D-5)/2} |\Gamma[(D-3)/2]| & D > 3 \\ A_n \times \left(\frac{r_{\min}}{L_n}\right)^{(D-3)/2} K_{(D-3)/2}\left(\frac{r_{\min}}{L_n}\right) & 0 < D \le 3 \end{cases}. \tag{2}$$

Figure 1 shows the examples of $B_n(r_d)$ at various D values. The shape of $B_n(r_d)$ becomes flatter in the limit of $r_d \to 0$ when D increases beyond $D = 4$.

Given the linear relationship between RI and local macromolecular mass density defined by the Gladstone–Dale equation,[71,72] quantification of the RI correlation function is actually a measure of the tissue structure

$$n = n_0 + \rho\alpha, \tag{3}$$

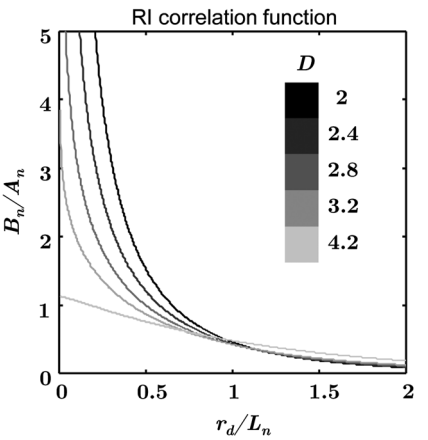

Fig. 1 Examples of $B_n(r_d)$ for different D values. r_d is normalized by the length scale L_n to be dimensionless.

where ρ is the local concentration of the solid material (e.g., macromolecules), and α is the RI increment, usually equals to 0.17 ml/g for biological materials. n_0 is the RI of water. Thus, $B_n(r_d)$ is not only a tissue RI correlation function, but it is also proportional to the correlation function of the spatial distribution of macromolecular density $B_\rho(r_d)$

$$B_\rho(r_d) = \alpha^{-2} B_n(r_d). \tag{4}$$

$B_\rho(r_d)$ is the most fundamental statistical measure of tissue ultrastructure. Accordingly, in this article, we refer to an alteration in tissue ultrastructure as a change in its $B_\rho(r_d)$ at the ultrastructural length scale.

With a defined $B_n(r_d)$, the differential scattering cross-section per unit volume $\sigma(\theta,\phi)$ can be obtained by a Fourier transform under the first-order Born approximation[66]

$$\sigma(\theta,\phi) = A_n \pi^{-\frac{1}{2}} 2^{\left(\frac{D}{2}-\frac{3}{2}\right)} \Gamma\left(\frac{D}{2}\right) k^4 L_n^3 \cdot \frac{[1-\sin^2(\theta)\cos^2(\phi)]}{\left\{1+\left[2kL_n \sin\left(\frac{\theta}{2}\right)\right]^2\right\}^{\frac{D}{2}}}, \tag{5}$$

where Γ is the gamma function, k is the wave number, and (θ,ϕ) is the polar and azimuthal angles of the scattering direction. Thus $\sigma(\theta,\phi)$ translates $B_n(r_d)$ into a measurable optical quantity, which in turn makes it possible to invert the measurements back to the structural properties. The condition for the Born approximation to be valid is[73]

$$\sigma_n^2 (kL_n)^2 \ll 1, \quad \text{when } kL_n \gg 1. \tag{6}$$

Optical properties are defined through $\sigma(\theta,\phi)$. The scattering coefficient μ_s is obtained as the integral of $\sigma(\theta,\phi)$ over the entire 4π angular space

$$\mu_s = \frac{1}{4\pi} \int_0^{2\pi} \int_0^{\pi} \sigma(\theta,\phi) \sin(\theta) \mathrm{d}\theta \mathrm{d}\phi. \tag{7}$$

The anisotropy factor g is the average cosine of the scattering angle of $\sigma(\theta,\phi)$

$$g = \frac{1}{\mu_s} \int_0^{2\pi} \int_0^{\pi} \sigma(\theta,\phi) \cos(\theta) \sin(\theta) \mathrm{d}\theta \mathrm{d}\phi. \tag{8}$$

The reduced scattering coefficient μ_s' is defined as

$$\mu_s' = \mu_s(1-g). \tag{9}$$

The backscattering coefficient μ_b is defined as

$$\mu_b = 4\pi\sigma(\theta=\pi). \tag{10}$$

All the above optical properties can be analytically expressed in terms of three parameters defining the RI correlation function,[66] which establishes the forward problem for the following inverse calculation. In biological tissue, the anisotropy factor is typically larger than 0.7 which implies $kL_n \gg 1$. In this regime, both μ_s' and μ_b are proportional to k^{4-D}. In the case of μ_s', this proportionality is only valid for $D<4$. When $D>4$, μ_s' is no longer dependent on wavelength. In the case of μ_b, there is no such limit. The conditioned functions of μ_b and μ_s' are[24,66]

$$\mu_b = A_n 2^{\left(\frac{D}{2}+\frac{1}{2}\right)} \pi^{\frac{3}{2}} \Gamma\left(\frac{D}{2}\right) L_n^{3-D} k^{4-D}, \qquad kL_n \gg 1 \tag{11}$$

$$\mu_s' = A_n b 2^{\left(\frac{3}{2}-\frac{D}{2}\right)} \pi^{\frac{1}{2}} \Gamma\left(\frac{D}{2}-1\right) L_n^{3-D} k^{4-D}, \quad kL_n \gg 1, 2<D<4, \tag{12}$$

$$\text{where } b = \frac{(D-2)[32+D(D-10)]}{(8-D)[24+D(D-10)]}.$$

The above two expressions are particularly useful because μ_s' can be measured in the diffused light regime by technique such as diffuse reflectance spectroscopy (DRS),[74,75] and μ_b can be measured in the ballistic region by technique such as reflectance confocal microscopy[76] or OCT.[27] Note that the above expressions of μ_b and μ_s' are limited forms when $kL_n \gg 1$. It is more accurate to use the complete analytical equations (see Refs. 24 and 57).

3.2 *ISOCT*

The OCT primarily detects the backscattering signal from tissue. By interfering the scattered field with a reference field, OCT generates the depth-resolved tomographic images of the scattering medium. The principle of ISOCT is that the interference of light scattered from the spatial variations of RI (e.g., tissue ultrastructures) within a 3-D resolution voxel results in detectable optical signals, which in turn can be used to inversely calculate the ultrastructural properties. By measuring the spectra of two fundamental optical parameters (μ_s and μ_b) for each voxel, the three structural parameters (σ_n^2 or A_n, L_n, and D) can be calculated according to the analytical expression [Eqs. (5)–(11)] introduced in Sec. 3.1.

We can take a first-order approximation and model the OCT A-line signal as[24]

$$I^2(z) = rI_0^2 L \frac{\mu_b(z)}{4\pi} \exp(-2z\mu_s), \tag{13}$$

where I_0 is the illumination intensity, r is the reflectance on the reference arm, L is the temporal coherence length of the source, and z is the geometric penetration depth in tissue. Note that z is proportional to the optical depth (d) by a scaling factor of $1/\langle n\rangle$, $z = d/\langle n\rangle$, where $\langle n\rangle$ is the mean RI of the medium (assumed to be 1.38 for biological tissue). The intensity decay rate along the depth is proportional to μ_s. The depth-resolved $\mu_b(z)$ is equal to

$$\mu_b(z) = \frac{4\pi I^2(z)}{rI_0^2 L} \exp(2z\mu_s). \tag{14}$$

In addition, the wavelength-dependent $I^2(z,k)$ can be obtained by a time-frequency analysis method on the OCT interferogram such as short-time Fourier transform (STFT).[77,78] Thus, the spectrum of $\mu_b(z,k)$ can be calculated.

This inverse method directly measures the spectra of two fundamental optical quantities: μ_b, and μ_s, and indirectly deduces the values of D, L_n, A_n or σ_n^2, and g. According to Eq. (11), the exponent of μ_b spectra is equal to 4-D, so that D can be calculated by fitting the μ_b spectra with a power law function of k. Then, L_n is a function of D and the ratio of $\mu_b(z)$ and μ_s, $a(z) = \mu_b(z)/\mu_s$, and can be calculated according to an equation

in Ref. 24. A_n or σ_n^2 can be calculated based on Eqs. (2) and (11). The value of g is a function of D and L_n and can be calculated according to the same equation reported previously.[66,70] The data-processing method is described in detail in Sec. 4.3.

4 Methods

4.1 *OCT System Setup*

To implement the ISOCT imaging system, we adopted an open-space Fourier-domain OCT (FDOCT) configuration with an illumination wavelength ranging from 650 to 800 nm (SuperK, NKT Photonics, Birkerød, Denmark). The laser was delivered by an optical fiber, collimated by a lens, and input into a cube beam splitter (Thorlabs, CM1-BS013, Newton, New Jersey) by which the light was divided into a sample arm and a reference arm. The reference arm consisted of a series of glass plates for dispersion control, and a mirror reflecting the light backward. The sample arm consisted of a two-dimensional (2-D) scanning mirror (Thorlabs, GVSM002, Newton, New Jersey) and an objective lens (effective NA = 0.04) to focus the light onto a specimen. The scanning range is 2×2 mm in the transverse plane (x, y) and each direction has 256 A-lines. We used a 2048 pixel line-scan camera (Aviiva, SM2, e2v, Milpitas, California) in a homemade spectrometer to capture the interference spectrum. The axial resolution was measured as ~2 μm in air and the transverse resolution was estimated to be ~10 μm. The depth of imaging was ~1.0 mm in tissue.

4.2 *Image Segmentation*

The OCT provided the 3-D volumetric images of tissue. In order to study the depth-resolved optical and ultrastructural properties from epithelium and stroma separately, we digitally delineated the surface of the tissue and segmented the crypts (composed of epithelial cells) and stroma from OCT images of colonic mucosa. The topical surface of the 3-D volumetric image of colonic mucosa was identified by the intensity gradient along the A-line signal. A threshold at 20% of the maximum intensity of a B-scan image was selected to binarize the image. The derivative of the binarized A-line was taken, and the peak locations marked the boundaries. In order to exclude the mucus and cell debris on top of the tissue surface, an iterative algorithm was designed as follows: after a boundary was detected, the average value of the next 30 pixels was calculated on the binarized A-line. If the averaged value was larger than 0.9 (averaged from the binarized signal), then the boundary location was recorded; otherwise, it was discarded. Then, the algorithm moved to the next boundary until the condition was met. This procedure was repeated on the B-scans, and thus the tissue surface was identified.

The segmentation of crypts and stroma in rectal mucosa was based on the intensity thresholding. We first created a 2-D gray-scale image using the mean intensity projection along a depth of ~200 to 350 μm from the surface. An intensity histogram adjustment was then performed to maximize the contrast. Next, a global image threshold calculated using Otsu's methods[79] was used to binarize the image. Closed areas smaller than ~40 μm^2 were removed as noise, and the perimeters of the closed areas were marked as the boundaries between the crypts and stroma. Finally, a rectangular region of interest (ROI) on the 2-D mean intensity projection image was manually selected based on visual confirmation of whether cryptal or stromal components could be separated by our segmentation algorithm. Within the ROI, the crypts and stroma were then digitally segmented for ISOCT analysis.

4.3 *ISOCT Signal Processing*

In order to calculate the optical (μ_b,μ_s, and g) and ultrastructural (D, L_n, and A_n) properties, we performed ISOCT signal processing on the raw FDOCT interference spectrum. The A-line signal with respect to the optical path was first obtained by a Fourier transform on the entire bandwidth of the interference spectrum. The optical path was then converted into geometric penetration depth z by using the mean RI of the medium (~1.38 in tissue). Next, the natural log of the A-line signal was fitted with a linear function of z. The slope is proportional to μ_s according to Eq. (13), and thus we calculated μ_s from the fitted slope. Next, the depth-resolved backscattering coefficient $\mu_b(z)$ was obtained by multiplying $\exp(2z\mu_s)$ to the square intensity of the A-line signal according to Eq. (14). To calibrate the measurements of μ_b and μ_s, microsphere aqueous phantoms with different microsphere diameters were prepared and imaged. The squared A-line intensity and the fitted slope were calibrated to μ_b and μ_s, which were predicted by Mie theory. The calibration data have been presented in our previous publication.[24]

Next, we calculated $D(z)$ using the following steps. A Gaussian spectral window with width $k_w = 0.36\ \mu m^{-1}$ was applied to the interference spectrum, and the A-line signal contributed by the selected band was obtained by a Fourier transform. The depth resolution was relaxed to ~20 μm due to the windowing. The corresponding $\mu_b(z)$ was obtained by the same method described above. This process was repeated with the Gaussian window sweeping through the whole spectral range, and thus the wavelength-dependent $\mu_b(z, k)$ was generated. Then, a power law function of k was fitted to the spectra of $\mu_b(z)$. The exponent is equal to 4-D according to Eq. (11), and thus we calculated the value of $D(z)$ from the fitted exponent.

Next, we deduced $L_n(z)$. The ratio of $\mu_b(z)$ and μ_s, $a(z) = \mu_b(z)/\mu_s$, was calculated. The value of L_n depends on D and a, and thus we obtained $L_n(z)$ with known $a(z)$ and $D(z)$ according to the equation as seen in the previous publication.[24]

Finally, $g(z)$ was calculated with $L_n(z)$ and $D(z)$ according to the same equation as in Refs. 66 and 70. Then, $A_n(z)$ was calculated according to Eq. (11) with known $\mu_b(z)$, $L_n(z)$, and $D(z)$, where k is taken at the central wavelength 710 nm.

4.4 *Ex Vivo Specimen Preparation*

Human *ex vivo* biopsies were obtained by following the protocol approved by NorthShore University Health System's Institutional Review Board, and all patients who provided samples gave informed consent. The normal-appearing rectal endoscopic biopsies were acquired during colonoscopies. If colonic polyps were found during the colonoscopy, then the polyps were retrieved for histopathological diagnosis. The ISOCT measurements were taken on the rectal biopsies. The duodenal biopsies were acquired from the peri-ampullary mucosa (1 to 3 cm from the ampulla) either during upper endoscopy procedures or from surgically resected Whipple specimens within 30 min of the Whipple procedure. Immediately after removal, the specimens were transferred to a phosphate-buffered saline (PBS) solution and refrigerated until measurement with ISOCT.

4.5 *Cell Preparation and HDAC Inhibition by VPA*

To introduce cell chromatin structural changes, we adapted an established *in vitro* model using valproic acid (VPA) to inhibit the DNA-histone binding, partly mediated by histone deacetylase (HDACs). HT-29 colon cancer cell lines were grown in McCoy's 5A medium (ATCC, Manassas, Virginia) mixed with 10% fetal bovine serum +50 mg/mL penicillin/streptomycin in a 5% CO_2 environment at 37°C. C-terminus Src kinase (CSK) shRNA-stably transfected HT-29 cells (CSK knockdown) were obtained and grown as previously described.[80] The CSK knockdown cells were treated with VPA (Sigma, St. Louis, Missouri) at a concentration of 1.5 mM for 4 h according to the protocol of previous publications.[81] For ISOCT measurements, cells were trypsinized from the culture dish and pelleted at 1000 rpm for 5 min in a centrifuge and transferred onto a glass slide for imaging. We estimated around 10 million cells to form a pellet. The thickness of the cell pellets was several hundred of microns, so that the reflection from the glass slide can be excluded in the STFT analysis. All measurements were completed within 15 min of trypsinization to ensure the cell viability.

4.6 *Collagen Gel Preparation and Cross-linking*

To mimic the collagen fiber network and to introduce ECM structural changes, we used a collagen *in vitro* model. Preparation of lysyl oxidase (LOX)-containing gels was adapted from a previously described protocol.[82] A 1.6-mg/mL collagen solution was prepared by mixing rat tail Collagen I (BD Biosciences, San Jose, California) with deionized water, 10× PBS (Sigma, 1:10 dilution), and 1-M NaOH (Sigma, 1:100 dilution) on ice. LOXL4 (Sigma) was added to the collagen to reach final concentrations of 0, 150, 200, or 350 μg/mL, and 50 μL of each solution was placed in a 16-well glass chamber slide (Thermo Scientific, Hanover Park, Illinois). Gels were incubated at 37°C for 1 h, after which 175 μL of 1× PBS was added to the top of each gel. The gels were incubated at 37°C for 5 days. Before OCT imaging, the supernatant PBS was removed by a pipette. Then, the gel was imaged from the glass chamber slide to avoid the unnecessary disturbance.

4.7 *Statistics*

All statistical data were plotted as mean ± the standard error. One-tailed, two-sample Student's *t*-tests were used to analyze the significance of the difference in CRC and PC fields carcinogenesis. A one-tailed *t*-test was used, since the directionality of the changes in optical and ultrastructural properties was established in a previous study.[22]

5 Results

In this section, we first compare the OCT images with the histology from rectal and duodenum samples (Sec. 5.1). Next, we present the 3-D segmentation results from rectal OCT images to separate epithelium and stroma (Sec. 5.2). We then present the ISOCT analysis on the optical and ultrastructural changes in these two tissue compartments in CRC field carcinogenesis (Secs. 5.3 and 5.4) as compared with PC field carcinogenesis (Sec. 5.5). Lastly, we present two in vitro experiments to confirm some of the mechanisms of the observed changes in cellular and extracellular components (Sec. 5.6).

5.1 *OCT Microscopic Representation for Rectal and Duodenal Specimens*

Figure 2 shows a comparison between the H&E-stained histological pictures and the OCT images from *ex vivo* rectal and duodenal specimens. The structure of colonic mucosa consists of a folded epithelial cell layer (crypts) surrounded by the stroma [lamina propria (LP)], as shown in Fig. 2(a). The colonic epithelial cells divide and proliferate from the base of the crypts and migrate to the cryptal apex until shedding into the colonic lumen. As we can see in Fig. 2(a), the epithelial cells at the base of the crypts have smaller sizes and pack more densely than the upper portion of the crypts. The top of the LP is covered by a single layer of matured epithelial cells around 20 to 30-μm thick, and some of the shedded cell debris can be observed. In

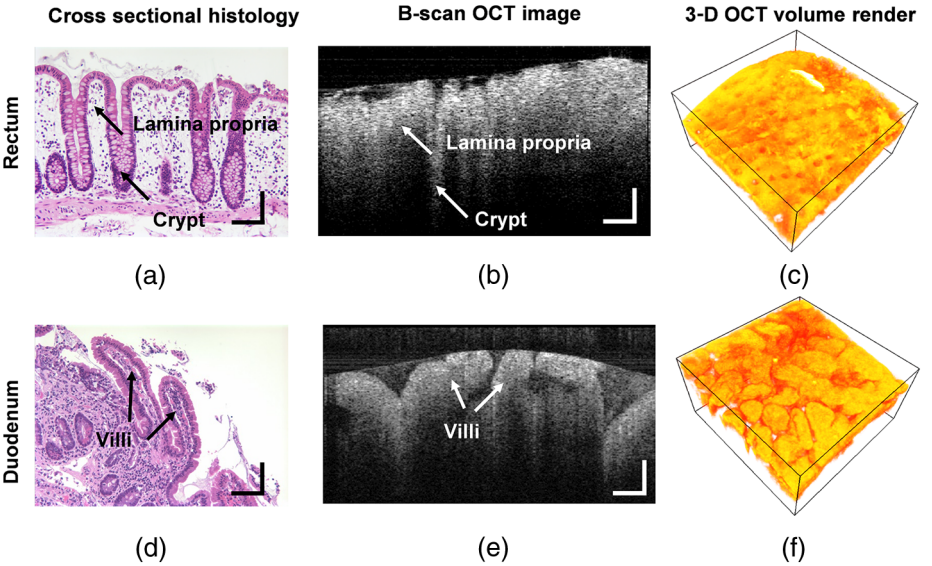

Fig. 2 H&E histology, OCT B-scan images, and three-dimensional (3-D) OCT volume render for (a–c) rectal and (d–f) duodenal biopsies. Bar = 0.2 mm.

LP, the primary component is a complex collagen network forming the ECM, within which there are also scattered stromal cells. Figure 2(b) shows the corresponding cross-sectional B-scan OCT image. The crypts can be seen as extending into the mucosa, and the LP can be seen as the surrounding tissue. A 3-D intensity rendering of a rectal sample is shown in Fig. 2(c).

A similar comparison for the duodenal specimen is shown in Figs. 2(d)–2(f). In the duodenum, the most prominent morphological features are the villi shown in Fig. 2(d). The villi consist of an outer shell of epithelial cells with LP filling the inside. The diameter of a villus is around 200 to 300 μm and the length can be as long as ~1 mm. From the OCT B-scan and 3-D images in Figs. 2(e) and 2(f), the randomly oriented villi structures were visualized. Using the comparison with histology, we confirmed that the OCT images acquired from rectal and duodenal specimens accurately measured the expected microscopic structures.

5.2 *Three-Dimensional Segmentation of Epithelium and LP*

Because the OCT images can accurately reconstruct the tissue microscopic features, we developed image segmentation methods to separate epithelial and LP components in rectal biopsies for later ISOCT analysis. As Fig. 3(a) shows, the tissue surface was detected using the intensity thresholding method described in Sec. 3.2. The red line in the B-scan image delineates the tissue boundary and defines the origin of the penetration depth $z = 0$. Thus, the penetration depth is the absolute depth with respect to the surface. We could also see that in deeper portions of the mucosa, the epithelium had a higher signal than LP, which creates contrast for a separation of the two compartments. Figures 3(b)–3(d) illustrates the segmentation method. We approximated epithelial structures as cylinders and took mean intensity projection from a slab of the volumetric data. We found that for depths between around $0.2\ \text{mm} < z < 0.35$ mm, the contrast between epithelium and LP was optimal. Figure 3(d) shows an example of the mean intensity projection map from $z = 0.2$ to 0.35-mm slab. Using a ROI exampled in the yellow square of Fig. 3(d), we applied our segmentation algorithm to separate the two tissue components as in Fig. 3(e) for further ISOCT analysis. The segmentation method is described in Sec. 3.2. With volumetric image processing, we can separate epithelium and LP in 3-D spaces and analyze their depth-resolved properties separately.

5.3 *Optical and Ultrastructural Changes in Epithelium and LP in CRC Field Carcinogenesis*

With 3-D imaging capability and image segmentation, we performed ISOCT analysis to quantitatively compare the changes in CRC and PC fields carcinogenesis.

We first investigated CRC field carcinogenesis on rectal biopsies. The CRC field carcinogenesis occurs in all segments of the colon, including the ascending, transverse, descending, and sigmoidal colon, and the rectum. Thus, we targeted the rectum as the surrogate site for the CRC field carcinogenesis because this region is the most accessible for CRC screening in the clinic. According to the colonoscopic findings and histopathological examination of retrieved colonic polyps, the patients were categorized into four groups as shown in Table 2: patients without any polyps present during colonoscopy (control group); patients with hyperplastic polyps (HPs), which are generally benign; patients harboring adenomatous (premalignant) polyps with polyp diameter less than or equal to 9 mm (adenoma); and patients harboring adenomatous polyps with polyp diameter greater than or equal to 10 mm [advanced adenomas (AA)]. It is important to note that not all adenomas

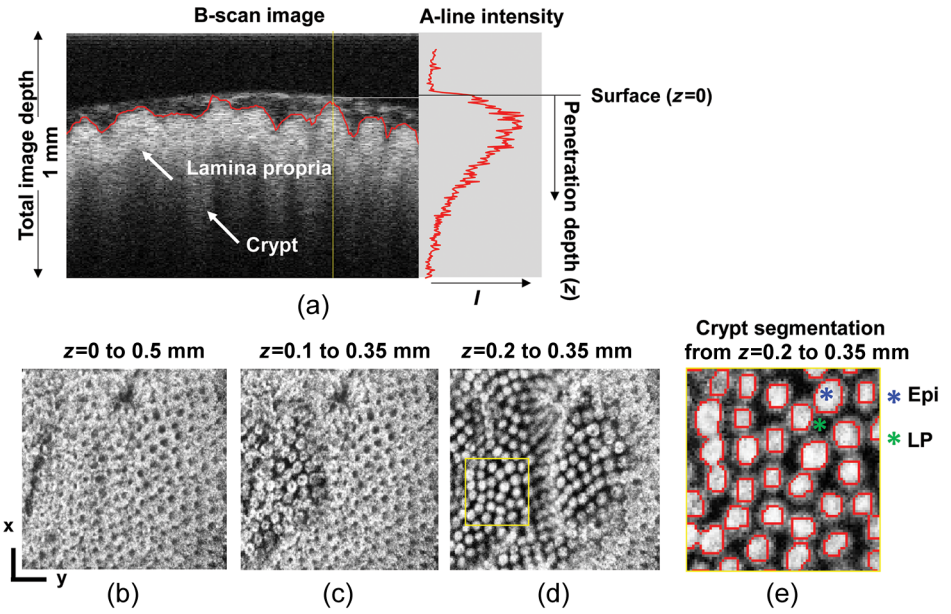

Fig. 3 Localization of epithelium (Epi) and lamina propria (LP) in 3-D spaces. (a) Tissue surface is identified and defined at $z = 0$; the origin of the penetration depth is from the tissue surface; one A-line signal is plotted to show the intensity change along the depth. (b–d) Mean intensity projection from slabs between different penetration depths. Bar = 0.2 mm. (e) Crypt segmentation from the ROI in (d). Epi and LP identified with blue and green asterisks.

Table 2 CRC study: patient characteristics.

Patient type	*n*	Age
Control	27	63 ± 8
HP	17	64 ± 10
Adenoma	20	64 ± 11
AA	21	65 ± 13

Note: HP hyperplastic polyp; AA advanced adenoma.

progress to cancer, but the risk of progression increases with adenoma size. Thus, adenomas are a biomarker of future CRC, and the risk progresses from control patients to those with adenoma and AA.

Using our segmentation methods discussed previously, we segmented 71 of the 85 patient biopsies: Control = 23, HP = 14, Adenoma = 16, and AA = 18. Other samples were deformed so that the epithelium and LP were unrecognizable from the image, possibly due to the mechanical stress during the pinch biopsy processing. Those samples were excluded from the following analysis.

The advantage of ISOCT in quantifying 3-D ultrastructural properties is illustrated in Fig. 4. Two representative examples of 3-D images from rectal biopsies in control and AA groups were pseudocolor coded by D. Qualitative comparison between rectal mucosae from AA and control patients [Fig. 4(a)] shows that the AA samples have an overall higher D. We could also see that there was a significant heterogeneity in the spatial distribution of D across the mucosa. To yield a more robust statistical analysis, we separately averaged the A-line signal from all crypts and LP within an ROI [see the definition in Sec. 4.2 and the example in Fig. 3(d)] and calculated μ_b and μ_s for the two tissue components. For each patient, the mean values of each parameter from several ROIs ($n \geq 3$) were taken. The image segmentation then allowed us to examine the depth-dependent changes in epithelium and LP in CRC field carcinogenesis.

Figure 5 shows the comparison between control and AA groups in both epithelium and LP compartments. Note again that the x-axis represents the penetration depth with respect to the surface. Epithelium and LP showed lower μ_b in the AA group than in the control [Figs. 5(a) and 5(d)]. μ_b at first increased to a local maximum of about ~40 μm, roughly at the depth of the basal membrane, but maintained a roughly constant value in deeper tissue. g was higher for AA in both epithelium and LP [Figs. 5(b) and 5(e)]. The separation was particularly dramatic in LP at depths greater than 100 μm. μ_s' [Figs. 5(c) and 5(f)] was smaller for the AA group in both epithelium and LP.

Next, we examined the ultrastructural changes quantified based on the W–M model. Both epithelium and LP from AA patients showed a higher D compared with that of control patients [Figs. 6(a) and 6(d)]. Epithelium showed a better contrast within the top 100-μm depth, whereas in LP, the greatest change was noted in deeper tissue >200 μm [Figs. 6(a) and 6(d)]. L_n did not appear to be appreciably different in epithelium between control and AA, but in LP, AA patients had elevated L_n for tissue depths around 100 to 200 μm. To compare the RI fluctuation magnitude, Figs. 6(c) and 6(f) show B_n ($r_d = 35$ nm) as a function of tissue depth. The value of 35 nm is the lower limit of length scale sensitivity of ISOCT, beyond which ISOCT can no longer detect ultrastructural alterations.[23] We note that at $r_d = 35$ nm, the RI fluctuations are weaker in AA group than in control [Figs. 6(c) and 6(f)].

5.4 *Depth-Resolved Changes in CRC Field Carcinogenesis*

The most significant optical and ultrastructural alterations in the epithelium and LP may occur at different depths. To identify the locations of the alterations in the epithelium and LP, we plotted the relative change in the optical and ultrastructural properties between AA to control groups and the corresponding p-values as a function of depth (Fig. 7). Because μ_b and D are two directly measured depth-resolved quantities, we used them as our representative markers. In epithelium, the contrast for D reached a maximum around ~65 μm in depth [Fig. 7(a)], and the depth range, where the difference was significant ($p < 0.05$), was from 50 to 75 μm [Fig. 7(c)]. In LP, the optimal contrast for D was from ~200 to 250 μm [Figs. 7(b) and 7(d)]. The p-values for μ_b are below 0.05 for all depths in both compartments.

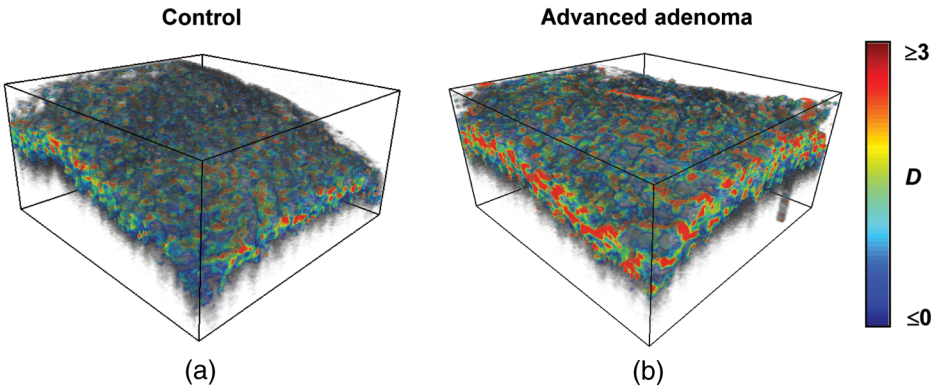

Fig. 4 Pseudocolor 3-D images encoded by D from representative rectal biopsies in (a) control and (b) advanced adenoma (AA) groups. The volume rendering intensity maps in grayscale are fused with the corresponding color-coded D map. The 3-D map is obtained after smoothing by $50 \times 50 \times 30$ μm 3-D median filter in $L \times W \times H$. Dimension: $2 \times 2 \times 1$ mm in $L \times W \times H$.

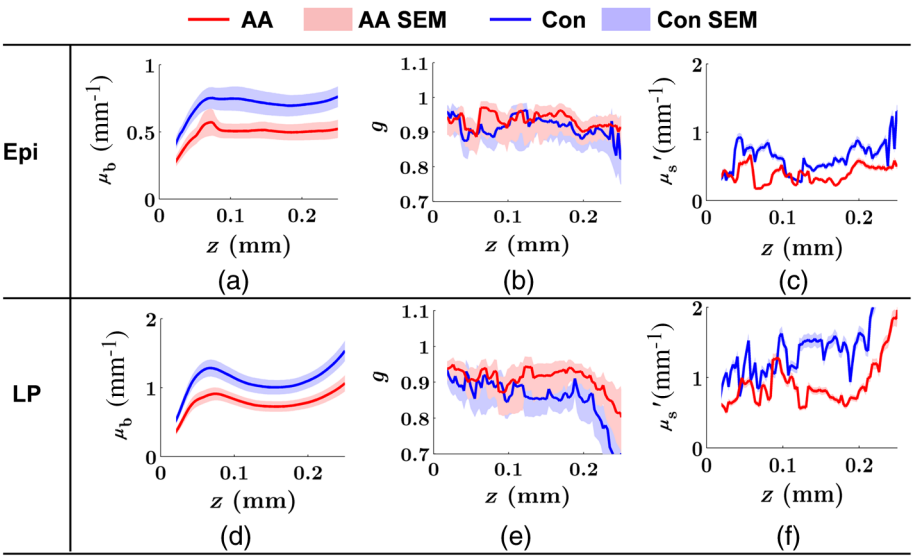

Fig. 5 Depth-resolved optical properties quantified in colorectal cancer (CRC) field carcinogenesis. The parameters were compared between control (Con) and AA groups separately in (a–c) epithelium (Epi) and (d–f) LP. The shadow areas show the standard error of the mean (SEM). The averaged g values were used for μ_s' calculation, and the SEM of μ_s' is calculated from μ_s measurements.

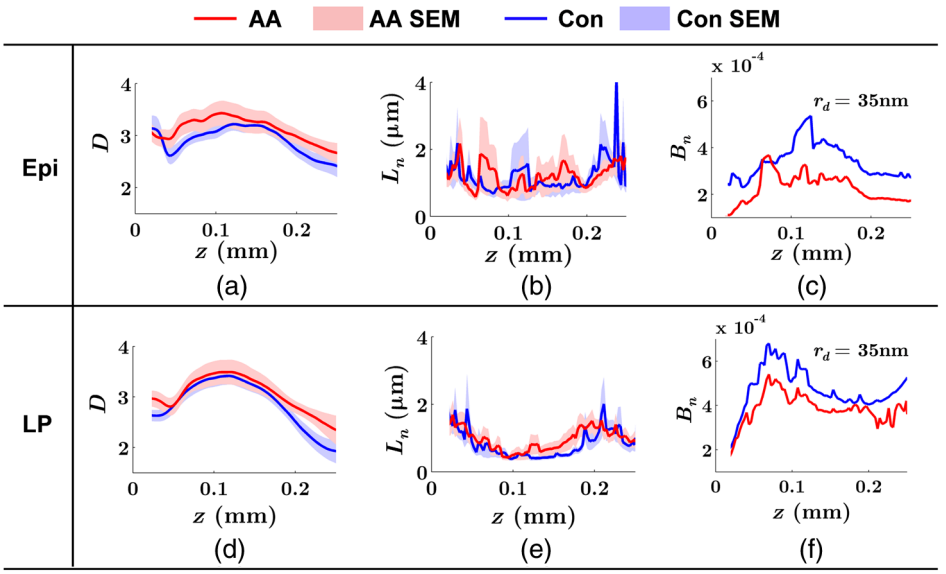

Fig. 6 Depth-resolved ultrastructural properties quantified in CRC field carcinogenesis. The parameters were compared between control (Con) and AA groups separately in (a–c) epithelium (Epi) and (d–f) LP. The shadow areas show the standard error of the mean (SEM). B_n is calculated at $r_d = 35$ nm by using the mean value of A_n, D, and L_n according to Eq. (1).

Having identified the location of the most significant alterations, we next examined whether the alterations parallel the progression of the severity of field carcinogenesis and the risk of carcinogenesis. As discussed in Sec. 4, we considered four groups of patients depending on colonoscopic findings: patients with no neoplastic lesions, patients with HPs (most carrying no malignant potential), patients with non-AAs, and finally those with AAs. Figure 8 shows the averaged values of the optical properties from 40 to 90-μm depth in epithelium and 200 to 250 μm in LP. Overall, the change in most of the optical properties paralleled the CRC risk from control patients to those with AAs and was consistent in both epithelium and LP: μ_b progressively decreased, g increased, μ_s and μ_s' decreased. While the change in the majority of the parameters reached statistical significance, a few parameters failed to reach $p < 0.05$ significance level (Fig. 8). This could be due to the biological variability with our finite sample size.

Figure 9 plots the average values of the ultrastructural properties D, L_n, and B_n ($r_d = 35$ nm) assessed from the same locations as in Fig. 8. Both in epithelium and LP, D increased and B_n

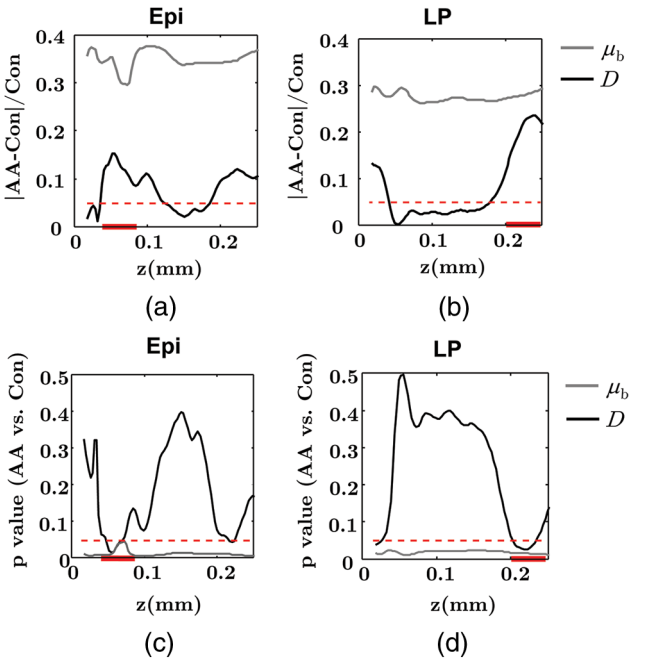

Fig. 7 Percent change and *p*-values of D and μ_b from AA group to control (Con) group, in (a and c) epithelium (Epi) and (b and d) LP. The dashed lines are labeled 5% level. The red bars on *x*-axis show the depth range where the averaged values are calculated for comparison in Figs. 8 and 9.

($r_d = 35$ nm) decreased progressively paralleling the risk of CRC from control patients to those with AA. There were no obvious trends for L_n. The values of L_n were around 1 μm.

5.5 *Optical and Ultrastructural Properties in PC Field Carcinogenesis*

A similar approach and data analysis were used to analyze the optical and ultrastructural alterations occurring in PC field carcinogenesis. While the pancreatic duct shows the diffuse carcinogenesis, directly instrumenting the pancreatic duct is fraught with complications. Several groups have shown that the peri-ampullary duodenum shares profound molecular changes (mutations/methylation) with the pancreatic duct in patients harboring PC.[83,84] Thus, we chose the peri-ampullary duodenum as the surrogate site for PC field carcinogenesis. The patients were categorized into two groups as shown in Table 3: control (no pancreatic neoplasia) and pancreatic adenocarcinoma (AC) according to the pathology report after the endoscopic examination.

Because the structure of duodenal villi is considerably more complicated than the cryptal morphology of rectal mucosa, the separation of epithelium and LP in the duodenal biopsies was impractical. Thus, we calculated the optical and ultrastructural properties of the duodenal biopsies as a combined effect of both components. Depth-resolved optical and ultrastructural changes from PC to control patients were plotted in Fig. 10. Using the similar method in CRC field carcinogenesis, we also identified significant alterations at two depth segments at about 30 to 80 μm and 170 to 220 μm in PC patients based on the changes in μ_b and D (Fig. 11). The averaged values of the optical and ultrastructural properties from the first segment are plotted in Fig. 12. A decrease in μ_b, μ_s', and B_n ($r_d = 35$ nm) and increase in D and g were observed in PC field carcinogenesis, which is consistent with the similar changes in CRC field carcinogenesis.

5.6 *Mechanisms for Intracellular and Extracellular Ultrastructural Changes*

In the previous sections, we investigated the histological location (epithelium versus LP and depth) and physical nature [$B_n(r_d)$] of the optical/ultrastructural changes in CRC and PC fields carcinogenesis. The next question is what causes these physical changes in terms of specific intra- and extracellular structures? As mentioned above, chromatin clumping and collagen cross-linking are two of the most common structural hallmarks in cancer. Both events are expected to lead to

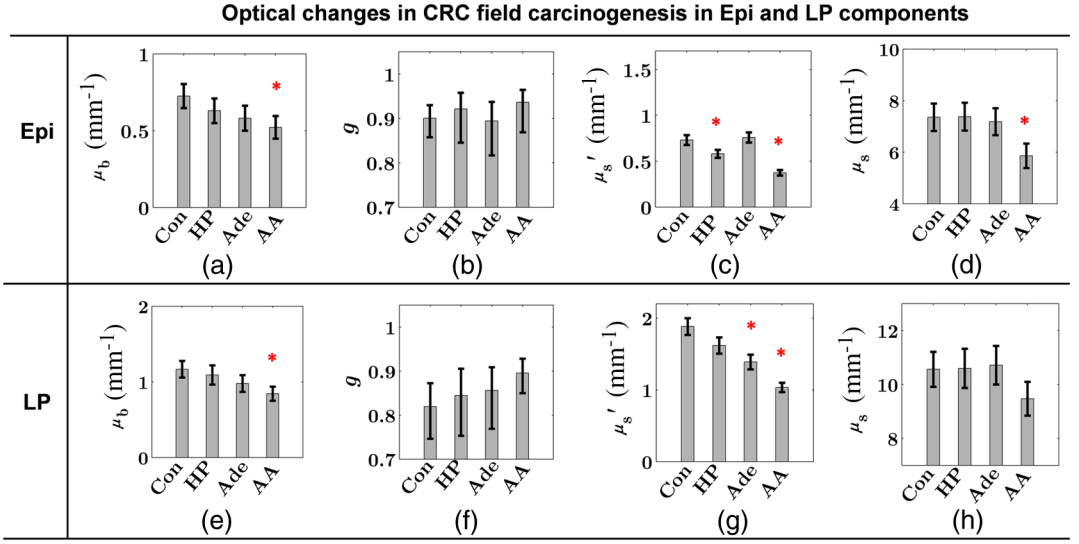

Fig. 8 Bar plots of optical properties in CRC field carcinogenesis. The averaged μ_b (a and e), g (b and f), μ_s' (c and g), and μ_s (d and h) were compared in four groups: control (Con), hyperplastic polyps (HPs); adenoma (Ade); and AA. Data were averaged at depth 40 to 90 μm in epithelium (Epi) and 200 to 250 μm in LP. *$p < 0.05$.

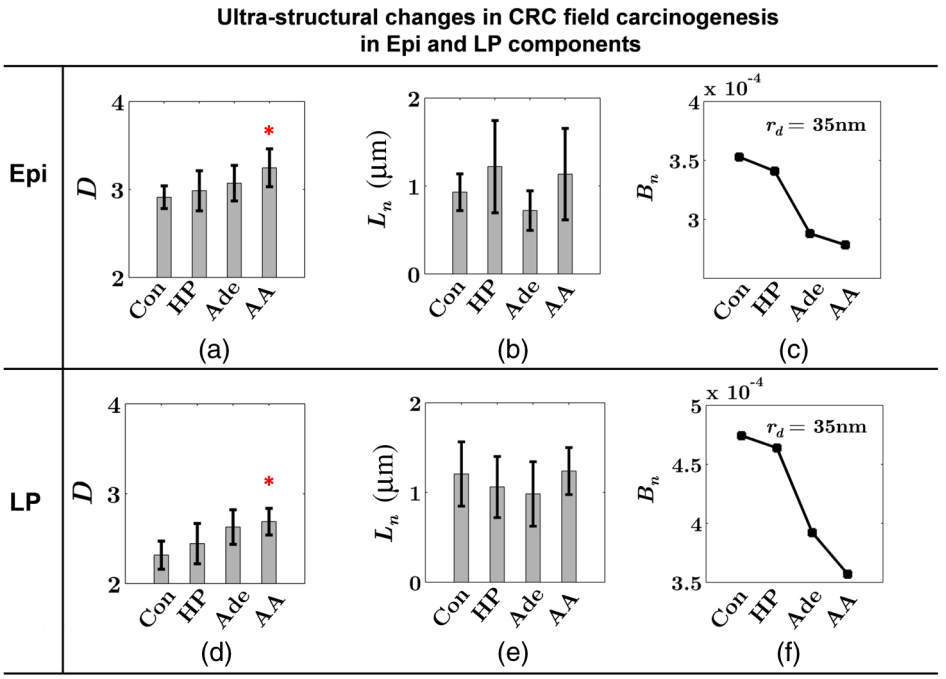

Fig. 9 Ultrastructural properties in CRC field carcinogenesis. The averaged D (a and d), L_n (b and e), and B_n ($r_d = 35$ nm) (c and f) were compared in four groups: control (Con), HPs; adenoma (Ade); and AA. Data were averaged at depth 40 to 90 μm in epithelium (Epi) and 200 to 250 μm in LP as marked in Fig. 7. *$p < 0.05$.

a shift of structural length scales to larger sizes in accordance with the change in $B_n(r_d)$ observed by ISOCT. Therefore, we tested whether those events could also play a role in the ultrastructural alterations in field carcinogenesis.

To alter the chromatin structure, we chose an aggressive variant of colon cancer cell line, CSK knockdown HT-29 cells, applied VPA to inhibit HDACs, and introduced chromatin relaxation. Chromatin compaction is partly mediated by HDACs,[85] a class of enzyme that allows the DNA to wrap around the histones. VPA is a drug known to have the effect of inhibiting HDACs, so that the VPA-retreated chromatin is less compacted.[81] The treatment was performed according to the established protocol with VPA concentration of 1.5 mM, as described in Sec. 4.5. The ISOCT measurements were performed on cell pellets (cell deposition after centrifuge) after 4-h treatment ($n = 9$ for both 0 and 1.5 mM VPA treatments), at which time point the effect of VPA approximately reached its maximum.[86] Figure 13(a) shows a decrease in D for cells treated with VPA. This suggests that the chromatin compaction manifests itself as an increase in D, in agreement with the field carcinogenesis alteration observed by ISOCT in the rectal epithelium.

Table 3 PC study: patient characteristics.

Patient type	n	Age
Control	7	59 ± 8
AC	15	70 ± 7

Note: AC adenocarcinoma.

To introduce changes in ECM, we used collagen fiber models of ECM and applied LOX to induce the collagen cross-linking. LOX alters collagen structure by promoting collagen cross-linking.[82] The gels were incubated with LOXL4 with increasing final concentration from 150 to 350 μg/mL. As in Fig. 13(b), D increased progressively from 2.1 ± 0.06 in control gels to 2.7 ± 0.18 in gels treated with 350 μg/mL LOXL4 ($n = 12$ for each treatment concentration). This experiment demonstrated that ECM collagen cross-linking induces an increase in D in agreement with the field carcinogenesis alteration observed by ISOCT in rectal stroma.

6 Discussion

In this article, we used ISOCT to study epithelial and stromal alterations in CRC as well as PC fields carcinogenesis. The ISOCT directly measures the spectra of two fundamental optical quantities, μ_b and μ_s, from which the 3-D distribution of the ultrastructural parameters D, L_n, and A_n or σ_n^2 are inversely calculated by modeling the autocorrelation function of the spatial distribution of RI in tissue using W–M family of functions. Furthermore, ISOCT can detect nanoscale alterations as small as 35 nm despite the typical microscale resolution of OCT by taking advantage of the significant contribution of subdiffractional length scales to the spectral behavior of μ_b.[23]

These properties make ISOCT well suited to detect the histologically unresolvable ultrastructural alterations in field carcinogenesis and to map the locations of these changes (e.g., epithelium versus stroma). Thus, we employed ISOCT to identify the ultrastructural alterations within the epithelium and stroma in CRC and PC fields carcinogenesis and to investigate the potential biological mechanisms responsible for these alterations.

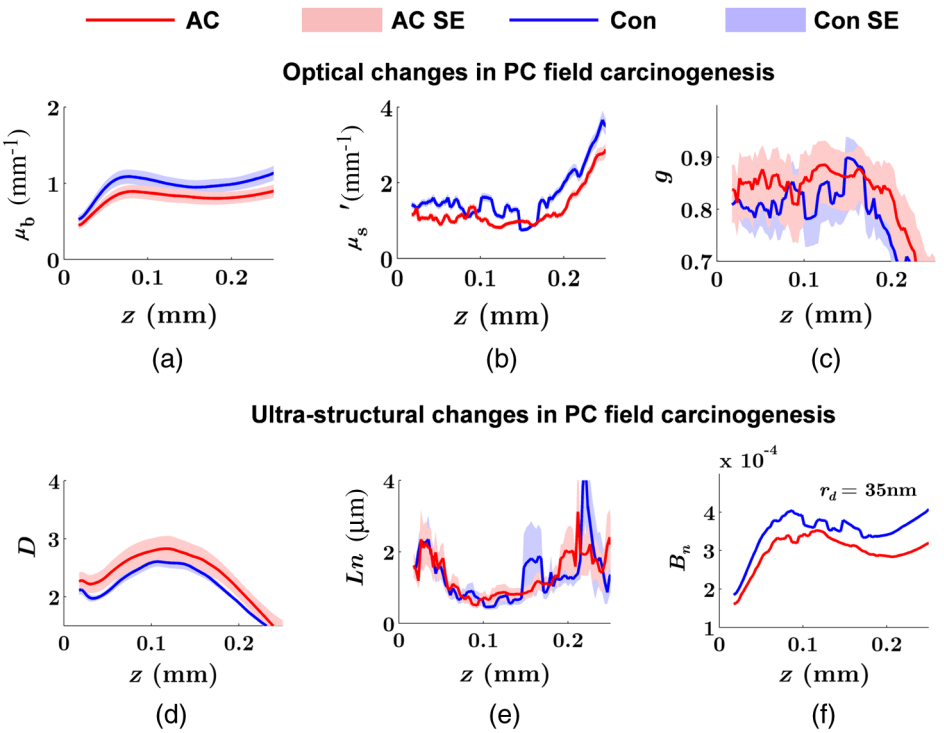

Fig. 10 Depth-resolved optical and physical properties of duodenum samples in pancreatic cancer (PC) field carcinogenesis. Comparison of control (Con) group and adenocarcinoma (AC) group for μ_b, μ_s', and g (a–c) and D, L_n, and B_n ($r_d = 35$ nm) (d–f). The shadow areas show the standard errors of the mean (SEM).

We observed that the optical and ultrastructural alterations were present in both the epithelium and stroma in CRC field carcinogenesis. The depth locations of the most significant changes in these two compartments were different. In the epithelium, the most significant increase in μ_b and D was observed at superficial depths less than 100 μm. Epithelial cells divide and proliferate from the base of the crypt (~500-μm deep) and migrate toward the lumen surface as they mature. Our data suggest that the mature epithelial cells located at superficial depths exhibit the most significant optical and ultrastructural changes. In the LP, the most significant changes in μ_b and D were observed at the depth range from 200 to 250 μm.

In addition to quantifying D, L_n, and A_n or σ_n^2, we compared the measured RI correlation functional forms from control and precancerous (field carcinogenesis) samples. This comparison illustrates the length scales of the ultrastructural alterations in field carcinogenesis. The overall shape of $B_n(r_d)$ was consistently "flatter" for field carcinogenesis of both CRC and PC corresponding to a shift of length-scale distributions to larger sizes, as shown in Fig. 14. This is expected in random media with

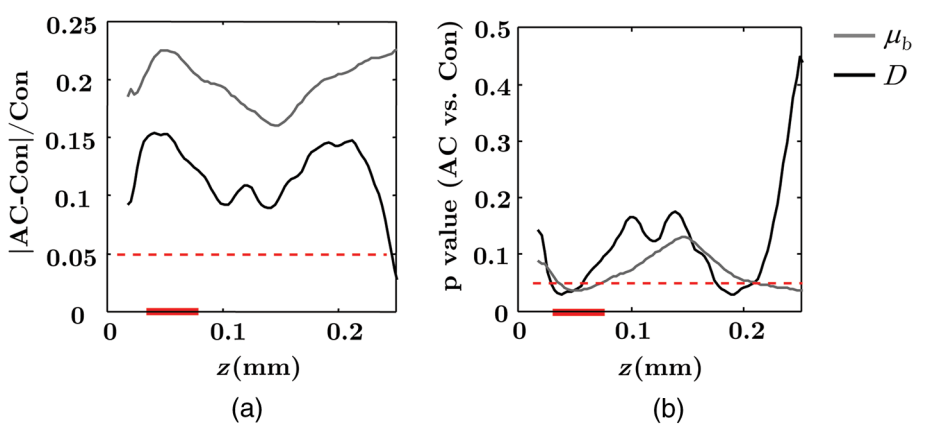

Fig. 11 (a) Relative changes and (b) p-values of D and μ_b from adenocarcinoma (AC) group to control (Con) group in duodenal specimen. The dashed lines are labeled 5% line. The red bars on x-axis show the depth range where the averaged values are calculated for comparison in Fig. 12.

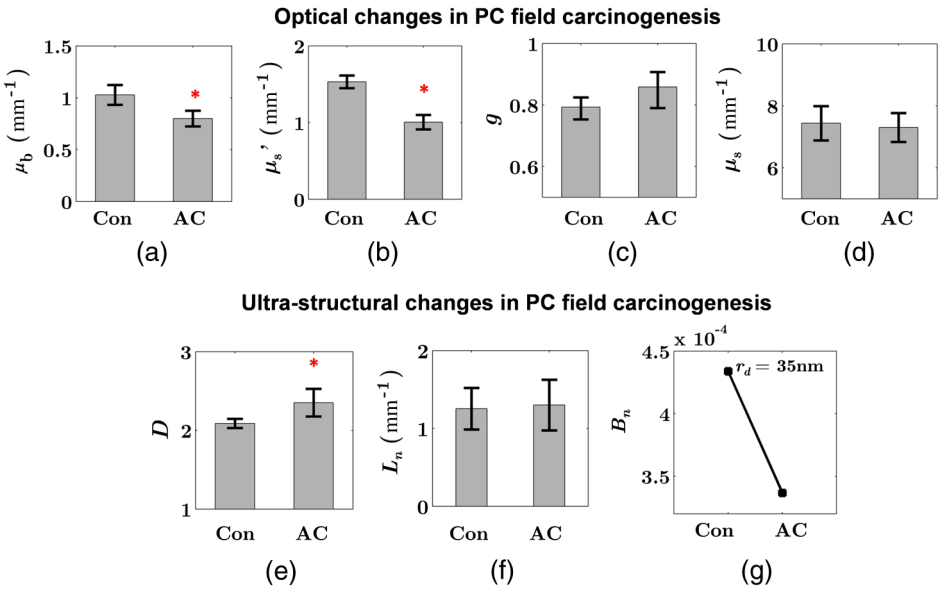

Fig. 12 Bar plots of (a–d) optical and (e–g) ultrastructural properties in PC field carcinogenesis. Con: control; AC: adenocarcinoma. Data were averaged at depth 30 to 80 μm. *$p < 0.05$.

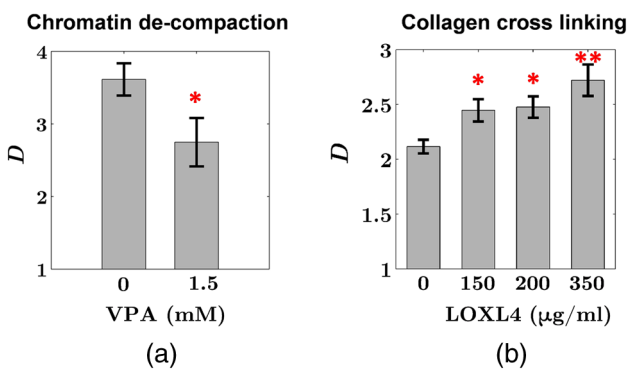

Fig. 13 *D* changes induced by (a) the de-compaction of chromatin structure and (b) the cross-linking of the collagen fiber network. Valproic acid (VPA) was used to inhibit histone deacetylases (HDACs) to relax chromatin. Lysyl oxidase (LOX4) was used to induce cross-linking of the collagen fibers. *D* analysis was performed on the signal averaged within the top 80 μm of the samples. *$p < 0.05$, **$p < 0.001$.

a higher-shape factor D, as we observed in our study. Importantly, the differences were mostly apparent at structural length scales smaller than ~0.8 μm (roughly the length scale of L_n). Above 0.8 μm, $B_n(r_d)$ for control and precancerous tissues was similar. This cutoff length scale is close to the resolution of conventional microscopy, which, in theory, is diffraction limited at ~350 nm, but in practice often closer to 1 μm due to light scattering within a histological section. This explains why in field carcinogenesis mucosa appears to be normal based on the criteria of microscopic histopathology (i.e., no microscopic alterations) despite the fact that it possesses ultrastructural alterations. On the other hand, ISOCT can be sensitive to the shape of a RI correlation function for length scales between ~35 and 450 nm,[23] beyond the resolution limit of conventional microscopes. At such small length scales, microscopy cannot resolve the deterministic structural features, though changes in the statistics of the RI correlation function can still be detected by ISOCT.

Because $B_n(r_d)$ ultimately determines the optical properties, the consistent changes of $B_n(r_d)$ in CRC and PC fields carcinogenesis should result in similar changes in the optical properties. Table 4 compares the trends in how optical and ultrastructural properties change in CRC and PC fields carcinogenesis. Indeed, in both CRC and PC, the ultrastructural alterations were consistent: a higher D and lower B_n ($r_d = 35$ nm). The optical changes were also consistent with a lower μ_b and μ_s' and higher g. This suggests that despite differences in molecular pathways, ultrastructural alterations are a common denominator of field carcinogenesis in different organ sites. Moreover, the changes observed by ISOCT are consistent with the previous *ex vivo* bench top[19,87] and *in vivo* LEBS probe system.[20,21] The lower μ_s' and higher D correspond to the LEBS enhancement factor E and spectral slope SS marker. The shapes of RI correlation functions in Fig. 14 are also similar to previous EBS studies in CRC and PC fields carcinogenesis.[22] It should be noted that although different optical techniques were applied to study the field carcinogenesis in these studies, the trends in the observed alterations of optical properties were found to be the same.

Having elucidated the physical nature of the ultrastructural alterations in CRC and PC fields carcinogenesis (i.e., a shift of length-scale distribution to larger sizes quantified by higher D), we used *in vitro* models to confirm that the chromatin compaction and collagen fiber cross-linking could cause D to increase in the epithelium and stroma, respectively. These results suggest that the changes known to occur at the dysplasia-to-neoplasia stages of carcinogenesis, i.e., chromatin clumping and ECM cross-linking, may develop considerably earlier in field carcinogenesis, albeit at a smaller, subdiffractional length scales, which may in part explain the increase in D observed in epithelium and LP in CRC field effect. The molecular mechanisms underlying the chromatin clumping include, most likely along with other pathways, HDACs upregulation. The *in vitro*

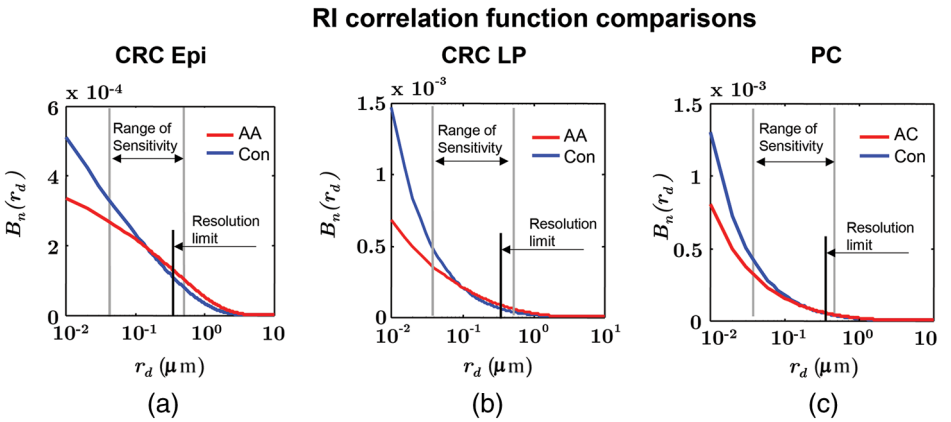

Fig. 14 Functional forms of $B_n(r_d)$ quantified in CRC and PC fields carcinogenesis. (a and b) The RI correlation functional form in epithelium (Epi) and LP from control (Con) and AA groups, respectively and (c) from control (Con) and adenocarcinoma (AC) groups. The functional forms were calculated according to Eq. (1) over the plotted length scale without leveling or truncation. The resolution limit of a conventional microscope (estimated at 350 nm with NA = 0.85, 600-nm illumination), and the sensitive length scale of ISOCT were also labeled.

Table 4 Comparison of changes observed in CRC and PC fields carcinogenesis.

	D	B_n (r_d = 35 nm)	μ_b	μ_s	g	μ_s'
CRC (AA versus control) in Epi	I*	De	De*	De*	I	De*
CRC (AA versus control) in LP	I*	De	De*	De	I	De*
PC (AC versus Control)	I*	De	De*		I	De*

Note: I increased; De Decreased; *$p < 0.05$.

data presented here are further supported by our recent study, which showed that the HDACs are upregulated in CRC field carcinogenesis and confirmed the associated chromatin compaction in epithelial cells in CRC field carcinogenesis.[57,58] The molecular mechanisms of ECM changes in field carcinogenesis still require further investigation but may potentially include pathways similar to those responsible for collagen cross-linking in tumor microenvironment such as LOX upregulation.

7 Conclusion

We observed the ultrastructural and optical changes in both epithelial cells and stroma in CRC field carcinogenesis. The epithelial and stromal alterations were consistent, although the most dramatic changes occurred at different depths within the mucosa. Optical changes in field carcinogenesis included a reduction in backscattering coefficient μ_b, a lower reduced scattering coefficient μ_s', and higher anisotropy factor g. Corresponding ultrastructural alterations included a change in the shape of RI correlation function: lower RI fluctuation and higher shape factor D of mass density correlation function. Furthermore, the alterations observed in both CRC and PC fields carcinogenesis were consistent and also consistent with previous *ex vivo* and *in vivo* studies using other optical techniques (e.g., LEBS and EBS). The ultrastructural alterations, in particular an increase in D, could be due, at least in part, to nanoscale manifestations of two classical microscopic events in carcinogenesis: chromatin clumping in epithelial cells and collagen cross-linking in stroma. Both these caused an increase in D in *in vitro* models. Future studies will have to elucidate the molecular causes and consequences of these events and their role in carcinogenesis.

Acknowledgments

The authors would like to acknowledge the grant support from both the National Institutes of Health (R01CA128641, R01CA165309, and R01CA156186) and the National Science Foundation (CBET-1240416). A. J. Radosevich is supported by a National Science Foundation Graduate Research Fellowship under Grant No. DGE-0824162. The author also would like to thank Benjamin Keane and Andrew Gomes for their help on the manuscript editing.

References

1. H. Chai and R. E. Brown, "Field effect in cancer–an update," *Ann. Clin. Lab. Sci.* **39**(4), 331–337 (2009).
2. D. P. Slaughter, H. W. Southwick, and W. Smejkal, "Field cancerization in oral stratified squamous epithelium; clinical implications of multicentric origin," *Cancer* **6**(5), 963–968 (1953).
3. W. A. Franklin et al., "Widely dispersed p53 mutation in respiratory epithelium. A novel mechanism for field carcinogenesis," *J. Clin. Invest.* **100**(8), 2133–2137 (1997).
4. L. Shen et al., "MGMT promoter methylation and field defect in sporadic colorectal cancer," *J. Natl. Cancer Inst.* **97**(18), 1330–1338 (2005).
5. H. Suzuki et al., "Epigenetic inactivation of SFRP genes allows constitutive WNT signaling in colorectal cancer," *Nat. Genet.* **36**(4), 417–422 (2004).
6. J. Mehrotra et al., "Quantitative, spatial resolution of the epigenetic field effect in prostate cancer," *Prostate* **68**(2), 152–160 (2008).
7. L. Nonn, V. Ananthanarayanan, and P. H. Gann, "Evidence for field cancerization of the prostate," *Prostate* **69**(13), 1470–1479 (2009).
8. L. J. Prevo et al., "p53-mutant clones and field effects in Barrett's esophagus," *Cancer Res.* **59**(19), 4784–4787 (1999).
9. G. Dakubo et al., "Clinical implications and utility of field cancerization," *Cancer Cell Int.* **7**(1), 1–12 (2007).
10. B. J. M. Braakhuis et al., "A genetic explanation of Slaughter's concept of field cancerization: evidence and clinical implications," *Cancer Res.* **63**(8), 1727–1730 (2003).

11. M. Endoh et al., "RASSF2, a potential tumour suppressor, is silenced by CpG island hypermethylation in gastric cancer," *Br. J. Cancer* **93**(12), 1395–1399 (2005).
12. P. S. Yan et al., "Mapping geographic zones of cancer risk with epigenetic biomarkers in normal breast tissue," *Clin. Cancer Res.* **12**(22), 6626–6636 (2006).
13. U. Utzinger et al., "Near-infrared Raman spectroscopy for *in vivo* detection of cervical precancers," *Appl. Spectrosc.* **55**(8), 955–959 (2001).
14. M. D. Keller et al., "Detecting temporal and spatial effects of epithelial cancers with Raman spectroscopy," *Dis. Markers* **25**(6), 323–337 (2008).
15. D. S. Alberts et al., "Karyometry of the colonic mucosa," *Cancer Epidemiol. Biomarkers Prev.* **16**(12), 2704–2716 (2007).
16. F. E. Robles et al., "Detection of early colorectal cancer development in the azoxymethane rat carcinogenesis model with Fourier domain low coherence interferometry," *Biomed. Opt. Express* **1**(2), 736–745 (2010).
17. A. Sharwani et al., "Assessment of oral premalignancy using elastic scattering spectroscopy," *Oral Oncol.* **42**(4), 343–349 (2006).
18. H. K. Roy et al., "Association between rectal optical signatures and colonic neoplasia: potential applications for screening," *Cancer Res.* **69**(10), 4476–4483 (2009).
19. V. Turzhitsky et al., "Investigating population risk factors of pancreatic cancer by evaluation of optical markers in the duodenal mucosa," *Dis. Markers* **25**(6), 313–321 (2008).
20. A. J. R. N. N. Mutyal et al., "*In-vivo* risk stratification of colon carcinogenesis by measurement of optical properties with novel lensfree fiber optic probe using low-coherence enhanced backscattering spectroscopy (LEBS)," presented at *Conf. 8230: Biomedical Applications of Light Scattering VI*, SPIE Photonics West, San Fransicso, CA (2012).
21. N. N. Mutyal et al., "*In-vivo* risk stratification of pancreatic cancer by evaluating optical properties in duodenal mucosa," in *Biomedical Optics and 3-D Imaging*, OSA Technical Digest, p. BSu5A.10, Optical Society of America, Miami, Florida (2012).
22. A. J. Radosevich et al., "Ultrastructural alterations in field carcinogenesis measured by enhanced backscattering spectroscopy," *J. Biomed. Opt.* **18**(9), 097002 (2013).
23. J. Yi et al., "Can OCT be sensitive to nanoscale structural alterations in biological tissue?" *Opt. Express* **21**(7), 9043–9059 (2013).
24. J. Yi and V. Backman, "Imaging a full set of optical scattering properties of biological tissue by inverse spectroscopic optical coherence tomography," *Opt. Lett.* **37**(21), 4443–4445 (2012).
25. J. Yi et al., "Inverse spectroscopic optical coherence tomography (ISOCT): non-invasively quantifying the complete optical scattering properties from week scattering tissue," in *Biomedical Optics and 3-D Imaging*, OSA Technical Digest, p. BTu3A.88, Optical Society of America, Miami, Florida (2012).
26. S. Bajaj et al., "915 development of novel optical technologies for early colon carcinogenesis detection via nanoscale mass density fluctuations: potential implications for endoscopic diagnostics," *Gastrointest. Endosc.* **75**(4), AB172 (2012).
27. D. Huang et al., "Optical coherence tomography," *Science* **254**(5035), 1178–1181 (1991).
28. A. F. Fercher et al., "Optical coherence tomography—principles and applications," *Rep. Prog. Phys.* **66**(2), 239–303 (2003).
29. D. Levitz et al., "Determination of optical scattering properties of highly-scattering media in optical coherence tomography images," *Opt. Express* **12**(2), 249–259 (2004).
30. J. M. Schmitt, A. Knüttel, and R. F. Bonner, "Measurement of optical properties of biological tissues by low-coherence reflectometry," *Appl. Opt.* **32**(30), 6032–6042 (1993).
31. F. J. van der Meer et al., "Localized measurement of optical attenuation coefficients of atherosclerotic plaque constituents by quantitative optical coherence tomography," *IEEE Trans. Med. Imaging* **24**(10), 1369–1376 (2005).
32. A. I. Kholodnykh et al., "Precision of measurement of tissue optical properties with optical coherence tomography," *Appl. Opt.* **42**(16), 3027–3037 (2003).
33. N. Bosschaart et al., "Measurements of wavelength dependent scattering and backscattering coefficients by low-coherence spectroscopy," *J. Biomed. Opt.* **16**(3), 030503 (2011).
34. C. Xu et al., "Characterization of atherosclerosis plaques by measuring both backscattering and attenuation coefficients in optical coherence tomography," *J. Biomed. Opt.* **13**(3), 034003 (2008).
35. V. M. Kodach et al., "Determination of the scattering anisotropy with optical coherence tomography," *Opt. Express* **19**(7), 6131–6140 (2011).
36. F. E. Robles, S. Chowdhury, and A. Wax, "Assessing hemoglobin concentration using spectroscopic optical coherence tomography for feasibility of tissue diagnostics," *Biomed. Opt. Express* **1**(1), 310–317 (2010).
37. N. Bosschaart et al., "Quantitative measurements of absorption spectra in scattering media by low-coherence spectroscopy," *Opt. Lett.* **34**(23), 3746–3748 (2009).
38. A. J. Radosevich et al., "Structural length-scale sensitivities of reflectance measurements in continuous random media under the Born approximation," *Opt. Lett.* **37**(24), 5220–5222 (2012).
39. T. McGarrity and L. Peiffer, "Protein kinase C activity as a potential marker for colorectal neoplasia," *Digest Dis. Sci.* **39**(3), 458–463 (1994).
40. T. J. McGarrity et al., "Colonic polyamine content and ornithine decarboxylase activity as markers for adenomas," *Cancer* **66**(7), 1539–1543 (1990).
41. I. Vucenik et al., "Usefulness of galactose oxidase-Schiff test in rectal mucus for screening of colorectal malignancy," *Anticancer Res.* **21**(2B), 1247–1255 (2001).
42. C. M. Payne et al., "Crypt-restricted loss and decreased protein expression of cytochrome c oxidase subunit I as potential hypothesis-driven biomarkers of colon cancer risk," *Cancer Epidemiol. Biomarkers Prev.* **14**(9), 2066–2075 (2005).
43. M. Anti et al., "Rectal epithelial cell proliferation patterns as predictors of adenomatous colorectal polyp recurrence," *Gut* **34**(4), 525–530 (1993).
44. C. Bernstein et al., "A bile acid-induced apoptosis assay for colon cancer risk and associated quality control studies," *Cancer Res.* **59**(10), 2353–2357 (1999).
45. L.-C. Chen et al., "Alteration of gene expression in normal-appearing colon mucosa of APCmin mice and human cancer patients," *Cancer Res.* **64**(10), 3694–3700 (2004).
46. C.-Y. Hao et al., "Altered gene expression in normal colonic mucosa of individuals with polyps of the colon," *Dis. Colon Rectum* **48**(12), 2329–2335 (2005).
47. H. Cui et al., "Loss of IGF2 imprinting: a potential marker of colorectal cancer risk," *Science* **299**(5613), 1753–1755 (2003).
48. C. R. Daniel et al., "TGF-α expression as a potential biomarker of risk within the normal-appearing colorectal mucosa of patients with and without incident sporadic adenoma," *Cancer Epidemiol. Biomarkers Prev.* **18**(1), 65–73 (2009).
49. T. Keku et al., "Local IGFBP-3 mRNA expression, apoptosis and risk of colorectal adenomas," *BMC Cancer* **8**(1), 143–151 (2008).
50. A. C. J. Polley et al., "Proteomic analysis reveals field-wide changes in protein expression in the morphologically normal mucosa of patients with colorectal neoplasia," *Cancer Res.* **66**(13), 6553–6562 (2006).
51. A. J. Gomes et al., "Rectal mucosal microvascular blood supply increase is associated with colonic neoplasia," *Clin. Cancer Res.* **15**(9), 3110–3117 (2009).
52. H. K. Roy et al., "Spectroscopic microvascular blood detection from the endoscopically normal colonic mucosa: biomarker for neoplasia risk," *Gastroenterology* **135**(4), 1069–1078 (2008).
53. H. K. Roy et al., "Optical measurement of rectal microvasculature as an adjunct to flexible sigmoidosocopy: gender-specific implications," *Cancer Prev. Res.* **3**(7), 844–851 (2010).
54. A. Albini, D. M. Noonan, and N. Ferrari, "Molecular pathways for cancer angioprevention," *Clin. Cancer Res.* **13**(15), 4320–4325 (2007).
55. R. Z. Chen et al., "DNA hypomethylation leads to elevated mutation rates," *Nature* **395**(6697), 89–93 (1998).
56. S. B. Baylin, "DNA methylation and gene silencing in cancer," *Nat. Clin. Pract. Oncol.* **2**(Suppl 1), S4–S11 (2005).
57. Y. Stypula-Cyrus et al., "HDAC up-regulation in early colon field carcinogenesis is involved in cell tumorigenicity through regulation of chromatin structure," *PLoS One* **8**(5), e64600 (2013).
58. Y. E. Stypula et al., "472 histone deacetylase (HDAC) expression as a biomarker for colorectal cancer (CRC) field carcinogenesis: role in high order chromatin modulation," *Gastroenterology* **144**(5), S-85 (2013).

59. A. Razin, "CpG methylation, chromatin structure and gene silencing–a three-way connection," *EMBO J.* **17**(17), 4905–4908 (1998).
60. F. Fuks, "DNA methylation and histone modifications: teaming up to silence genes," *Curr. Opin. Genet. Dev.* **15**(5), 490–495 (2005).
61. N. A. Bhowmick, E. G. Neilson, and H. L. Moses, "Stromal fibroblasts in cancer initiation and progression," *Nature* **432**(7015), 332–337 (2004).
62. L. Ge et al., "Could stroma contribute to field cancerization?" *Med. Hypotheses* **75**(1), 26–31 (2010).
63. T. L. Ratliff, "TGF-β signaling in fibroblasts modulates the oncogenic potential of adjacent epithelia," *Science* **303**(5659), 848–851 (2004).
64. J. M. Schmitt and G. Kumar, "Optical scattering properties of soft tissue: a discrete particle model," *Appl. Opt.* **37**(13), 2788–2797 (1998).
65. C. Amoozegar et al., "Experimental verification of T-matrix-based inverse light scattering analysis for assessing structure of spheroids as models of cell nuclei," *Appl. Opt.* **48**(10), D20–D25 (2009).
66. J. D. Rogers, İ. R. Çapoğlu, and V. Backman, "Nonscalar elastic light scattering from continuous random media in the Born approximation," *Opt. Lett.* **34**(12), 1891–1893 (2009).
67. J. Schmitt and G. Kumar, "Turbulent nature of refractive-index variations in biological tissue," *Opt. Lett.* **21**(16), 1310–1312 (1996).
68. C. J. R. Sheppard, "Fractal model of light scattering in biological tissue and cells," *Opt. Lett.* **32**(2), 142–144 (2007).
69. M. Xu and R. R. Alfano, "Fractal mechanisms of light scattering in biological tissue and cells," *Opt. Lett.* **30**(22), 3051–3053 (2005).
70. J. D. Rogers et al., "Modeling light scattering in tissue as continuous random media using a versatile refractive index correlation function," *IEEE J. Sel. Top. Quantum Electron.* **20**(2), 1–14 (2014).
71. H. G. Davies et al., "The use of the interference microscope to determine dry mass in living cells and as a quantitative cytochemical method," *Q. J. Microsc. Sci.* **s3-95**(31), 271–304 (1954).
72. R. Barer and S. Tkaczyk, "Refractive index of concentrated protein solutions" *Nature* **173**, 821–822 (1954).
73. İ. R. Çapoğlu et al., "Accuracy of the Born approximation in calculating the scattering coefficient of biological continuous random media," *Opt. Lett.* **34**(17), 2679–2681 (2009).
74. G. Zonios et al., "Diffuse reflectance spectroscopy of human adenomatous colon polyps *in vivo*," *Appl. Opt.* **38**(31), 6628–6637 (1999).
75. R. Doornbos et al., "The determination of *in vivo* human tissue optical properties and absolute chromophore concentrations using spatially resolved steady-state diffuse reflectance spectroscopy," *Phys. Med. Biol.* **44**(4), 967–981 (1999).
76. M. Huzaira et al., "Topographic variations in normal skin, as viewed by *in vivo* reflectance confocal microscopy," *J. Invest. Dermatol.* **116**(6), 846–852 (2001).
77. R. Leitgeb et al., "Spectral measurement of absorption by spectroscopic frequency-domain optical coherence tomography," *Opt. Lett.* **25**(11), 820–822 (2000).
78. F. E. Robles and A. Wax, "Measuring morphological features using light-scattering spectroscopy and Fourier-domain low-coherence interferometry," *Opt. Lett.* **35**(3), 360–362 (2010).
79. N. Otsu, "A threshold selection method from gray-level histograms," *IEEE Trans. Syst. Man Cybern.* **9**(1), 62–66 (1979).
80. D. P. Kunte et al., "Down-regulation of the tumor suppressor gene C-terminal Src kinase: An early event during premalignant colonic epithelial hyperproliferation," *FEBS Lett.* **579**(17), 3497–3502 (2005).
81. O. H. Kramer et al., "The histone deacetylase inhibitor valproic acid selectively induces proteasomal degradation of HDAC2," *EMBO J.* **22**(13), 3411–3420 (2003).
82. A. M. Baker et al., "Lysyl oxidase enzymatic function increases stiffness to drive colorectal cancer progression through FAK," *Oncogene* **32**(14), 1863–1868 (2012).
83. H. Matsubayashi et al., "Age- and disease-related methylation of multiple genes in nonneoplastic duodenum and in duodenal juice," *Clin. Cancer Res.* **11**(2), 573–583 (2005).
84. H. Matsubayashi et al., "DNA methylation alterations in the pancreatic juice of patients with suspected pancreatic disease," *Cancer Res.* **66**(2), 1208–1217 (2006).
85. A. J. Bannister and T. Kouzarides, "Regulation of chromatin by histone modifications," *Cell Res.* **21**(3), 381–395 (2011).
86. E. W. Y. Tung and L. M. Winn, "Epigenetic modifications in valproic acid-induced teratogenesis," *Toxicol. Appl. Pharmacol.* **248**(3), 201–209 (2010).
87. H. Roy et al., "Spectral slope from the endoscopically-normal mucosa predicts concurrent colonic neoplasia: a pilot *ex-vivo* clinical study," *Dis. Colon Rectum* **51**(9), 1381–1386 (2008).

Biographies of the authors are not available.